JOURNAL OF GEOPHYSICAL RESEARCH, VOL. 94, NO. C1, PAGES 995–1011, JANUARY 15, 1989

Quantification of Sand Bar Morphology: A Video Technique Based on Wave Dissipation

T. C. LIPPMANN AND R. A. HOLMAN

College of Oceanography, Oregon State University, Corvallis

A technique is presented to remotely measure the scales and morphology of natural sand bars based on the preferential dissipation of wind waves and swell over the crests of the bar. Photographic or video images are recorded and statistical uncertainties associated with incident wave height modulations removed by averaging (time exposures). Ground truth testing of the technique was carried out as part of the SUPERDUCK experiment in October 1986. The time exposures generally provided a good mapping of underlying morphology, allowing detection of the bar and determination of cross-shore and longshore length scales. However, during high waves, persistent surface foam obscures the relationship of image intensity to local dissipation (modeled theoretically by dissipation of a random wave field), and an enhancement technique of image differencing must be done to remove the bias. Errors in the estimate of bar crest distance from the shoreline are generally less than 35%, but this value depends on the geometry of the particular bar. Logistic simplicity and quantitative capabilities make this technique very attractive.

INTRODUCTION

Offshore sand bars are common features of the world's coastlines. The accumulation of sediment into large-scale features makes them an important, as well as interesting, sediment transport region. They are also very dynamic. While annual cycles in sediment deposition are observed on most coastlines (with offshore transport tending to form bars during higher energy wave conditions in winter months), significant morphological changes also occur on a much shorter time scale, especially in response to storms.

The physical processes that contribute to the dynamics of barred beaches are clearly not as simple as for plane beaches. Yet the new information available from studying these more complicated environments may provide valuable clues into the nature of the fluid-sediment interaction. In particular, cross-shore and longshore length scales of bars may potentially be related to fluid parameters if appropriate dynamical models are available.

The literature contains a number of models for bar generation by fluid motions. It has been hypothesized that linear bars are formed at the breaker location of plunging incident waves [*Keulegan*, 1948; *Shepard*, 1950; *Miller*, 1976], or under nodes or antinodes of waves standing against the shoreline [*Carter et al.*, 1973; *Lau and Travis*, 1973; *Short*, 1975; *Bowen*, 1980]. Hypotheses exist for the formation of three-dimensional crescentic [*Bowen and Inman*, 1971], welded, and apparently aperiodic sand bars, based, for example, on the interaction of phase-locked edge waves [*Holman and Bowen*, 1982]. Yet, surprisingly, these models are largely untested under natural conditions.

There are several reasons why field tests have not been accomplished. Proper measurement of the low frequency "surf beat," invoked by several of the models, requires sophisticated analysis techniques to resolve particular trapped (edge waves) and leaky modes. Though this technique requires a more extensive array of instrumentation than originally thought, it is now feasible [*Huntley et al.*, 1981; *Oltman-Shay and Guza*, 1987].

Measuring the morphology over large enough spatial scales and short enough time scales remains a major difficulty, exacerbated by the scientific emphasis on storm periods when bar evolution is occurring most rapidly. Traditionally, bar measurements are made using in situ field techniques that, due to hostile conditions in the surf zone environment, are not always easily applied. Also, the large scale of most bar forms requires extensive surveying both cross-shore and alongshore, typically on the order of many hundreds of meters. Nonstationarity may lead to errors if the bar moves significantly during the surveying period. Hastening the surveying process can eliminate bar stationarity problems, but not without the inevitable loss in spatial resolution and the potential introduction of spatial aliasing.

We have developed a remote sensing technique that allows the visualization and subsequent quantification of nearshore morphology based on the patterns of incident wave breaking. The premise of the technique is that more waves break over the shallows of the bar than surrounding areas. The sharp contrast between breaking and nonbreaking regions may be imaged photographically; however, instead of using an instantaneous "snapshot," we employ a long time exposure, thereby averaging out fluctuations due to incident wave modulations and giving a statistically stable image of the wave breaking pattern. Figure 1 illustrates the technique. The breaking wave pattern in Figure 1*a* suggests the presence of a sand bar, but the poor spatial coverage provided by breaking crests and the statistical uncertainty associated with natural modulations in wave height render the details of the bar morphology uncertain. In Figure 1*b* the breaking pattern has been averaged over a 10-min period in a time exposure. This image yields a much clearer view of the bar. Spatial coverage is both extensive and of high resolution. Nonstationarity problems are avoided, since the sampling interval (10 min) is substantially less than the observed time scales of appreciable bar movement [*Sallenger et al.*, 1984]. Finally, the logistics of the remote measurement technique are not constrained by high-energy surf zone con-

Paper number 88JC03642.
0148-0227/89/88JC-03642$05.00

Fig. 1*a*

Fig. 1*b*

Fig. 1. (*a*) Oblique snapshot of wave breaking on October 10, 1986, at low tide during the SUPERDUCK experiment. (*b*) A 10-min time exposure from the same date and tide. The white band at the shoreline is the dissipation maximum corresponding to the shore break, while the band offshore indicates the presence of a sand bar.

ditions and can be utilized wherever an adequate vantage point is accessible.

There has been some work on this problem as early as the 1940s using aerial photography [e.g., *Wiegel*, 1947; *Lundall*, 1948; *Harris and Umbach*, 1972], however with large uncertainties resulting from the small number of infrequent observations and limited knowledge of the precise connection between instantaneous visual wave breaking patterns and underlying topography. Our approach will greatly improve these estimates and allow for quantitative evaluation of the technique.

Our discussion of the technique will start with the theoretical background. To understand the relationship between the light intensity patterns observed in time exposure images and the underlying morphology, we make a working assumption that light intensity will vary as the dissipation of the incident waves. Modeling of dissipation over arbitrary topography using the random wave model of *Thornton and Guza* [1983] then gives guidance to the expected performance of the technique (while measured light intensity profiles turn out to be very similar to calculated profiles of dissipation, lending support to our assumption, we do not actually test this hypothesis by measuring wave dissipation).

Following the theory is a section on the photogrammetry involved in the transformation of oblique images. The theo-

retical resolution and accuracy of the technique are then discussed, followed by a description of our field methods and laboratory digitization techniques using a computerized image processor. Finally, we will discuss field tests based on field data from the 1986 SUPERDUCK experiment [*Crowson et al.*, 1988].

THEORY

The patterns of light intensity that are recorded in the time exposure photographs are a result of the bubbles and foam of breaking waves. To relate this visible signal to the fluid motions (and hence the underlying bar morphology), we must make some assumption about the mechanism of bubble formation. For the purposes of this paper we will hypothesize that the light intensity recorded on the film, $I(x,y)$, is simply proportional to the local incident wave energy dissipation $\varepsilon(x,y)$,

$$\langle I(x,y)\rangle \propto \langle \varepsilon(x,y)\rangle \tag{1}$$

where the angled brackets indicate time averaged. Since models of dissipation over a barred profile suggest a strong dependence of local dissipation on underlying morphology, dissipation may serve as a proxy measure of the nearshore topography.

We will approach the problem through the energy flux balance,

$$\frac{\partial}{\partial x}(Ec_g) = \frac{\partial}{\partial x}\left[\left(\frac{1}{8}\rho g H_{\text{rms}}^2\right) c_g\right] = \langle \varepsilon \rangle \tag{2}$$

where ρ is density, g is the acceleration due to gravity, E is the wave energy density, and c_g is the group velocity.

The simplest representation of waves shoaling on a beach assumes that the incident energy is narrow banded and can be represented by a single frequency f and wave height H_{rms}. Outside the surf zone, dissipation is through bottom friction. This is small compared with the dissipation due to surf zone breaking [*Thornton and Guza*, 1983] and provides no surface signal for imaging. Thus we take wave energy flux Ec_g to be conserved outside the breaker line. Inside the surf zone, wave height is assumed depth limited, similar to solitary wave theory [*McCowan*, 1891] or monochromatic lab results [*Galvin and Eagleson*, 1965] and supported by field tests [*Thornton and Guza*, 1982],

$$H_{\text{rms}}(x) = \gamma h(x) \qquad x < x_b \tag{3}$$

where x_b is the position of the breaker line and h is the still water depth. Thus wave energy flux is strictly a function of depth, and local dissipation is simply determined from the flux gradient (equation (2)). Dissipation over an arbitrary beach profile can easily be calculated using (2) and (3).

This monochromatic representation of the wave field, while simple, has several distinct disadvantages. First, if taken strictly, wave heights should actually increase as waves propagate from the bar crest into the deeper water of the trough. However, this nonphysical result can be simply avoided if, as a wave is numerically shoaled, the criterion for whether it is breaking is based on a "local" wave height, calculated by inviscid shoaling from the point immediately offshore. The second problem with the monochromatic model (more severe for our application) is that the maximum dissipation will generally be at the initial break point. This is, again, a nonphysical result, as well as an unfortunate one for our technique, since we are interested in using the intensity signal to determine the location of the bar crest, not the break point. However, this problem, which also occurs in the theory of longshore currents [*Thornton and Guza*, 1986], can be corrected by considering a random wave model where wave energy is considered composed of a distribution of waves with heights that are described statistically [*Thornton and Guza*, 1983]. For the remainder of the paper we will focus on the random wave model.

Random Wave Model

Models for the shoaling and breaking of random wave fields have been published by a number of authors [*Collins*, 1970; *Battjes*, 1972; *Kuo and Kuo*, 1974; *Goda*, 1975; *Battjes and Janssen*, 1978; *Thornton and Guza*, 1983]. These models consider the wave energy to be composed of a distribution of waves of varying height. The analysis is then carried out statistically, representing the waves in terms of probability distributions whose bulk properties may be found by integration. Many of these models invoke depth-limited breaking to determine dissipation (equation (2)). However, the latter two [*Battjes and Janssen*, 1978; *Thornton and Guza*, 1983] specify dissipation and use (2) in the opposite direction to find wave height. We will follow the analysis of *Thornton and Guza* [1983] (hereafter TG83).

Using the extensive data set from the Nearshore Sediment Transport Study (NSTS), TG83 showed that the wave heights H of a random incident wave field were well described by a Rayleigh probability distribution,

$$p(H) = \frac{2H}{H_{\text{rms}}^2}\exp\left[-\left(\frac{H}{H_{\text{rms}}}\right)^2\right] \tag{4}$$

which is an implied function of local depth, and hence of cross-shore distance. Surprisingly, this result was found to be valid throughout the entire nearshore region, including the surf zone where the underlying assumptions of linearity are clearly violated.

As the wave field shoals, some portion of the waves begin to break, modifying the distribution. The form of this modification is the main distinguishing feature of the above-listed random wave models. TG83 are unique in that their model for the shoaling of the wave height distribution is based on field data from a barred beach (Soldier's Beach, California) wherein the wave height time series were augmented with a record of which waves were actually breaking. They express the probability distribution of breaking waves $p_b(H)$ as a weighting of the distribution of all waves,

$$p_b(H) = W(H)\,p(H) \tag{5}$$

where, from the data, they determine the best form of the weighting function to be

$$W(H) = \left(\frac{H_{\text{rms}}}{\gamma h}\right)^2\left\{1 - \exp\left[-\left(\frac{H}{\gamma h}\right)^2\right]\right\} \tag{6}$$

They then model the dissipation of a breaking wave based on a periodic bore model [*Stoker*, 1957; *Hwang and Divoky*, 1970],

$$\varepsilon = \frac{f}{4}\rho g\frac{(BH)^3}{h} \tag{7}$$

where B is an empirical breaker coefficient, roughly representing the fraction of the bore face that is covered with foam. The mean dissipation $\langle\varepsilon\rangle$ is then the integral through the breaking wave height distribution,

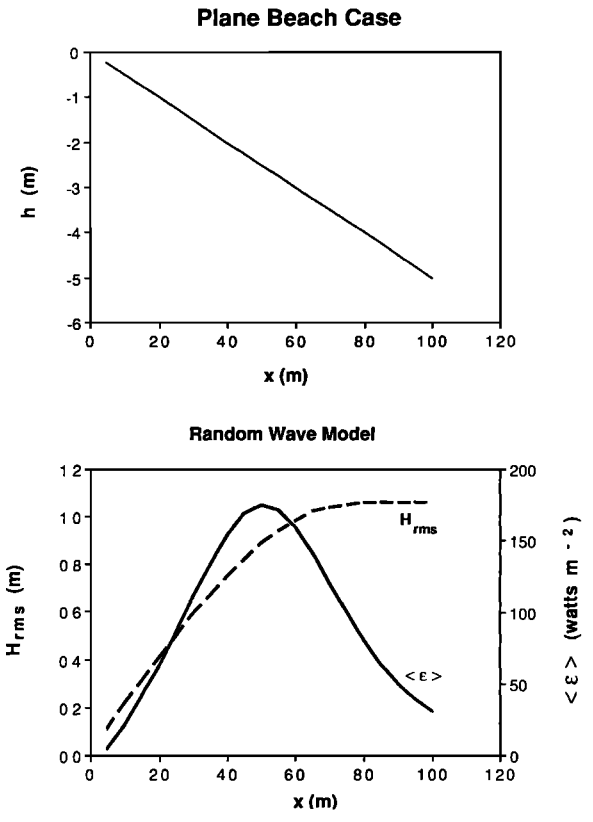

Fig. 2. Model results as waves are shoaled over a plane beach profile (top panel). The behavior of H_{rms} and $\langle\varepsilon\rangle$, plotted against offshore distance, is shown for the random wave model in the bottom panel.

$$\langle\varepsilon\rangle = \frac{3\pi^{1/2}}{16}\rho g B^3 f \frac{H_{rms}^5}{\gamma^2 h^3}\left[1 - \frac{1}{\left(1 + \left(H_{rms}/\gamma h\right)^2\right)^{5/2}}\right] \quad (8)$$

Application of the Model

Numerical implementation of the random wave model was carried out to determine the behavior of dissipation over various profiles, and to provide a comparison for field tests, to be discussed later in the paper. The energy flux balance (2) forms the basis for the model. TG83 note that in testing a variety of numerical schemes, the simplest forward stepping technique was found to be sufficiently accurate. We will use this same algorithm,

$$Ec_{gx}|_2 = Ec_{gx}|_1 + \langle\varepsilon\rangle|_1 \Delta x \quad (9)$$

Starting from the deepest grid point (assuming a wave height that has been linearly shoaled from deep water), the wave energy flux is stepped landward. For the random wave model, the flux at any shoreward point, labeled 2, is calculated using the flux and dissipation (equation (8)) found at the next seaward point, labeled 1. Note that the shallow water assumption is valid for all cases examined. Values used for B and γ are 1.54 and 0.42, respectively, taken as representative of field data [TG83].

Examples

Theoretical dissipation profiles have been calculated for three beach profiles. The first, a plane beach, is the simplest beach profile and provides a good illustration of the behavior of wave dissipation over unperturbed topography. The second, Torrey Pines beach (the site of the NSTS results) was used first to check the model results against TG83 (an error check of the programming) and, second, to show the sensitivity of dissipation to minor perturbations in an otherwise simple profile. Finally, a barred profile from the SUPERDUCK experiment was used to show the ability of dissipation (and hence the time exposure technique) to highlight the bar crest location. The latter case was also used to provide an understanding of the ground truth studies, conducted during SUPERDUCK, that will be discussed later.

Figure 2 shows the behavior of the random wave model on a plane beach profile, shown in the top panel. The model shows a single broad dissipation maximum offshore, resulting from the distribution of wave heights with some dissipation arising offshore due to the more energetic waves while most waves break near a finite break point. There is a dissipation maximum (albeit broad) despite the fact that the beach profile is plane. The area under the curve must equal the deep water energy flux.

Figure 3 shows the model results for Torrey Pines beach on October 20, 1978, during the NSTS experiment. This day was chosen as one of the two data runs analyzed in TG83 against which we could check the functioning of our model. Again, the beach profile is shown in the top panel, with associated H_{rms} and $\langle\varepsilon\rangle$ curves for and random wave model shown in the lower panel. Since the distribution of dissipation is dependent on local water depth, peaks of dissipation

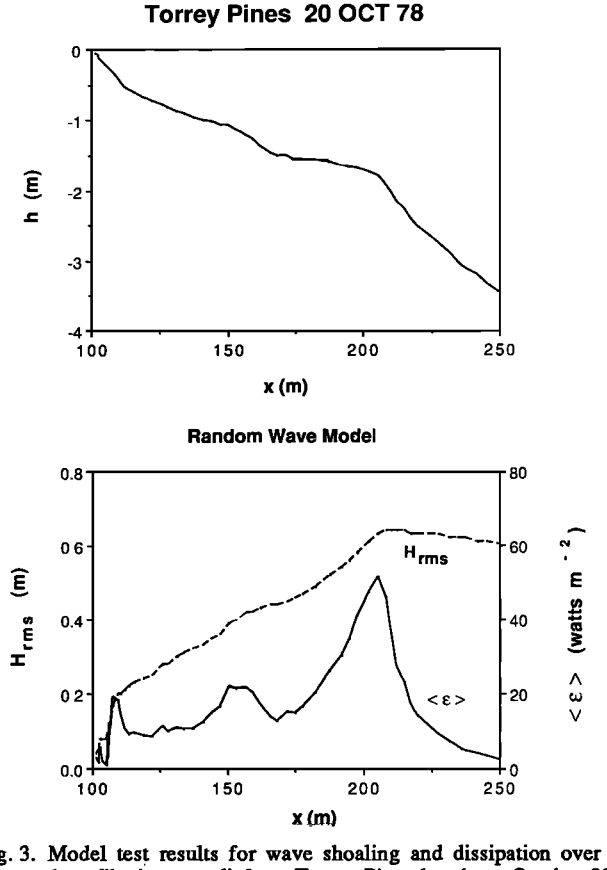

Fig. 3. Model test results for wave shoaling and dissipation over a surveyed profile (top panel) from Torrey Pines beach on October 20, 1978. The cross-shore behavior of H_{rms} and $\langle\varepsilon\rangle$ are shown for the random wave model in the lower panel.

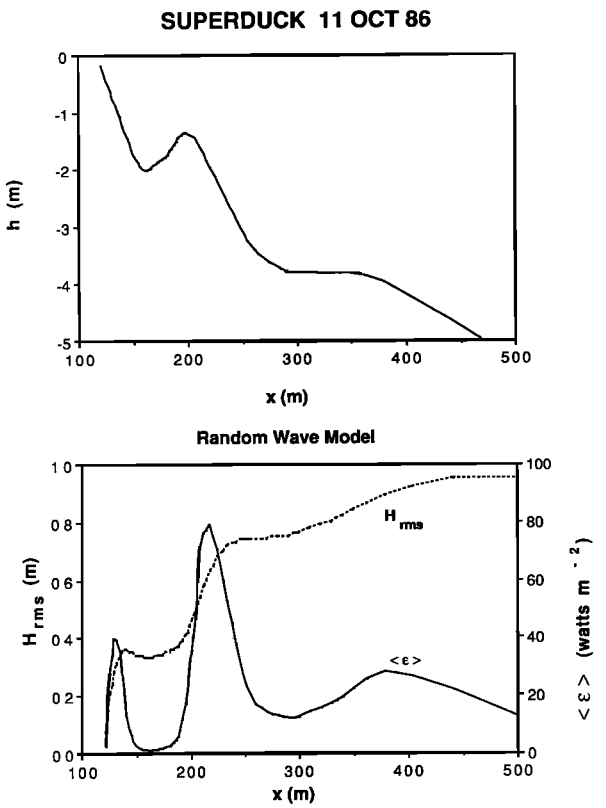

Fig. 4. Model results for wave shoaling and dissipation over a barred beach profile (top panel) from SUPERDUCK on October 11, 1986. The cross-shore behavior of H_{rms} and $\langle\varepsilon\rangle$ are shown for the random wave model in the lower panel.

will reflect positive changes of slope ("bumps" in the perturbation profile). The model indeed yields a well-defined dissipation peak over the large offshore bump located at x = 200 m. Thus it appears that the imaging of dissipation may prove useful in determining the horizontal length scales of perturbations (sand bars, terraces) in the bathymetry.

Figure 4 shows wave shoaling and dissipation for a barred beach profile (actually a linear storm bar which formed during the SUPERDUCK experiment). A second perturbation 375 m offshore is the residual of a semipermanent second linear bar. Three features are apparent in the dissipation curves. Offshore, the presence of the second bar (perturbation) is indicated by the random wave curve by a small dissipation peak, shoreward of which dissipation is lower but not zero. This is similar to the results for the low-tide terrace on Torrey Pines beach. The well-developed inner bar is clearly highlighted by the dissipation curve. However, the location of maximum dissipation is displaced seaward from the measured bar crest (location of minimum depth) by 20 m, a result of weighting the dissipation toward the larger waves. Continuing landward, the trough is indicated by a region of essentially zero dissipation. This contrast between the large dissipation over the bar and zero over the trough distinguishes (at least qualitatively) the signal due to sand bar morphology from that of a terrace or more minor perturbation. Finally, we see a narrow dissipation maximum near the shoreline, a feature that also shows up in the field tests discussed later. While the presence of this "shorebreak" maximum is reasonable, the details of its location may be poorly reproduced, since our dissipation model artificially forces wave height to zero at the shoreline (we allow no standing wave component).

The influence of deep-water significant wave height H_0 on the random wave model is shown in Figure 5. For any offshore position, it appears that an increase in H_0 will result in an increase in local RMS wave height H_{rms} up to a maximum value which depends on depth. Further increases in H_0 have no effect, and the local wave field is said to saturate. This behavior shows the merging of the dissipation-based model of shoaling used here with earlier depth-limited models for depths that are "shallow" with respect to the wave height, a point that was also made theoretically in TG83.

Variation of wave period T will affect the model in two ways. The deep water energy flux (hence area under the dis-

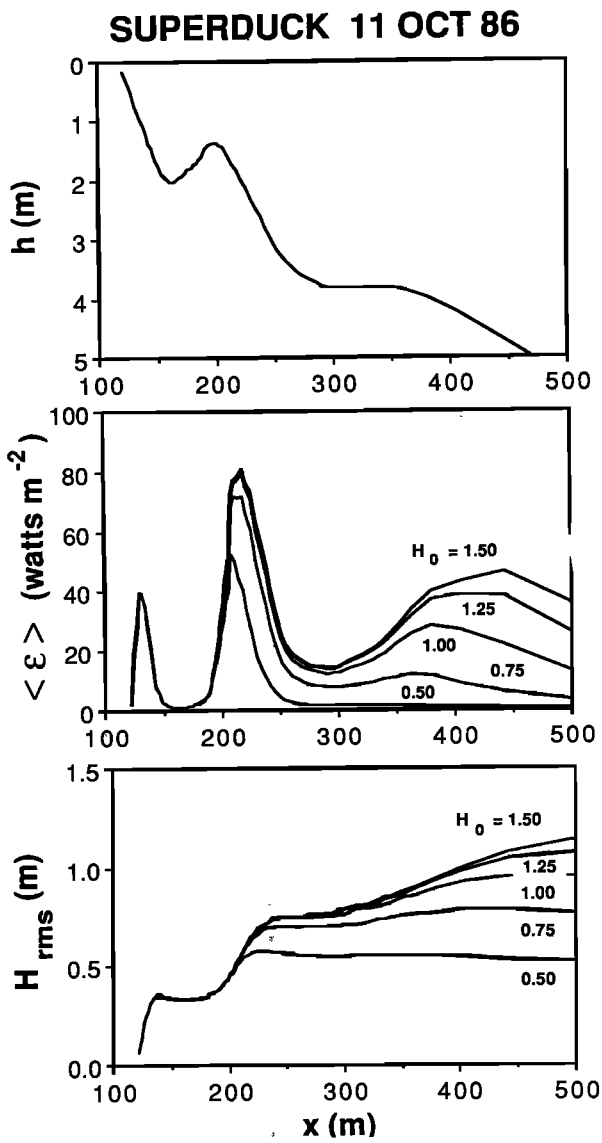

Fig. 5. Influence of deep-water rms wave height H_0 over a barred beach profile (top panel) from SUPERDUCK on October 11, 1986. The effect of increasing H_0 on dissipation, $\langle\varepsilon\rangle$, and local wave height H_{rms} at offshore locations is shown in the middle and lower panels, respectively.

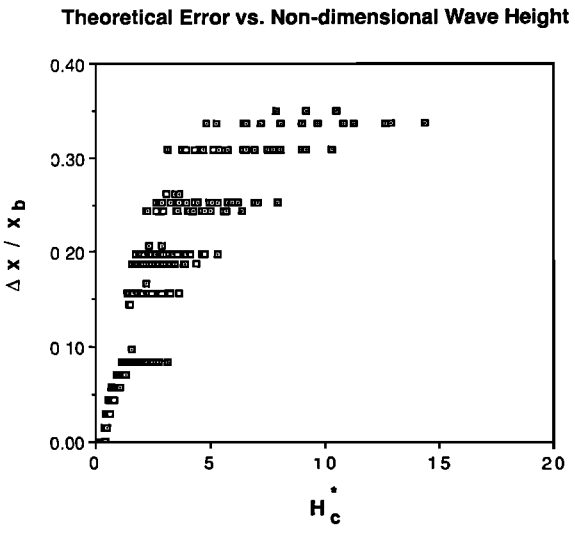

Fig. 6. Fractional error in locating the bar crest from theoretical dissipation maxima plotted against nondimensional wave height H_c^*.

sipation curve) depends linearly on T. Also, the dissipation (equation (8)) is inversely proportional to T. The net result is that dissipation profiles for different wave periods have different magnitudes but the same structure, including location and shape of peaks.

The saturation behavior of dissipation is beneficial to our objective of locating sand bar features, since the location of the offshore dissipation maximum is only weakly sensitive to offshore wave parameters. This is quantified in Figure 6, which shows the fractional error in locating the bar crest (difference between the location of the offshore dissipation maximum and the measured bar crest position Δx, divided by the offshore distance to the bar crest at mean tide x_c) versus the nondimensional wave height,

$$H_c^* = \left(\frac{H_0}{\gamma h_c}\right)\left(\frac{k_c}{2k_0}\right)^{1/2} \tag{10}$$

The variables h_c and k_c refer to the depth and local wave number at the bar crest, and k_0 is the deep-water wave number. H_c^* is derived by shoaling the deep-water energy flux to the bar crest, if wave breaking were not allowed (note that the second term in (10) is the shoaling coefficient). Figure 6 shows that the fractional error in locating the bar crest varies from 0% for small waves that just break over the bar (H_c^* = 0.5–1.0) to about 35% for a saturated wave field.

The above analysis suggests that if the visible intensity signal recorded in time exposure photographs does depend on incident wave dissipation, then the time exposure technique should work. Best results will occur for waves which just break over the bar, but even for larger waves the error in bar location identification will reach a maximum value, 35% for the above case. If the results are to be used to test bar generation models based on standing wave motions, wherein the bar location x_c scales as

$$\chi_c \equiv \frac{\sigma^2 x_c}{g\beta} \tag{11}$$

where β is the effective beach slope and $\sigma = 2\pi f$ is the radian frequency, then errors of less than 18% will occur in the predicted frequency f of the standing wave. It should be noted that this value is just from one sample geometry and would be different for different beach profiles. For instance, the value of x_c does not enter into the dimensional error Δx, so that for bars that are farther offshore the error would be smaller, and vice-versa. Similarly, for larger h_c (such as for higher tides), H_c^* would be smaller, and for higher tides, x_c would be larger. Both would tend to yield smaller relative errors. Again, the opposite is also true, so that for lower tides and smaller h_c, estimates will tend to be worse.

Photogrammetry

We wish to use oblique images to quantify the offshore and longshore length scales of the sand bar (and potentially other variables). Although photogrammetric equations for transforming images have been developed [e.g., *Okamoto*, 1982], the necessary equations will be derived here for completeness.

The location of any object in the image is a function of the spatial orientation of the camera in relation to ground topography and can be determined by a simple analysis of the geometry. We will outline the equations that define the transformation between image coordinates and ground coordinates. When transforming from ground to image coordinates the equations are fully defined. However, since the image is two-dimensional while the ground is three-dimensional, the opposite process (called rectification) is underdetermined. This is overcome by assuming one dimension to be known. For example, in rectifying images of waves the vertical coordinate is assumed to be at sea level; errors of the order of the wave amplitude are assumed negligible compared to the height of the camera.

The geometry and labeling conventions used in the rectification process are shown in Figure 7. Image coordinates will be denoted with small letters (x,y), and ground coordinates will be denoted with capital letters (X,Y). The optic center of the camera is located at point O, a distance Z_c above the x-y (ground) plane. The camera nadir line intersects the ground at the nadir N. The image points lie in the focal plane, which for our purposes will be considered the 1:1 positive, consistent with traditional photogrammetry conventions. The focal plane is separated from O by the focal length f_c, determined by the camera lens. The optic axis intersects the center of the focal plane at point p,

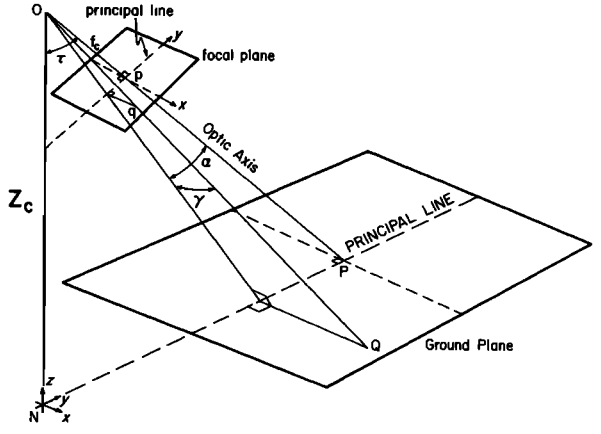

Fig. 7. Geometry and labeling conventions used for photogrammetry.

called the principal point, and forms an angle τ (the camera tilt) with the vertical nadir line. The principal line passes through the principal point and bisects the focal plane. The principal point is also the origin for the image coordinate system with the principal line as the y axis. The nadir point acts as the origin for the camera coordinate system with the principal line in the ground plane defining the positive y axis.

The ground location of any point Q is determined from its image coordinates (x_q, y_q) by

$$X_Q = Z_c \sec(\tau + \alpha) \tan\gamma$$

$$Y_Q = Z_c \tan(\tau + \alpha) \tag{12}$$

where the angles α and γ are defined as

$$\alpha = \tan^{-1}\left(\frac{y_q}{f_c}\right)$$

and (13)

$$\gamma = \tan^{-1}\left(\frac{x_q}{\sqrt{y_q^2 + f_c^2}}\right)$$

Transformation in the opposite direction, from ground to image points, is done by simply inverting and combining (12) and (13) to yield

$$y_q = f_c \tan\left(\tan^{-1}\left(\frac{Y_Q}{Z_c}\right) - \tau\right)$$

and (14)

$$x_q = \left(\frac{y_q^2 + f_c^2}{Z_c^2 + Y_Q^2}\right)^{1/2} X_Q$$

Several complications arise in applying these relationships in the field. First, these equations are a function of the camera tilt and focal length. Field measurement of tilt may be awkward and inaccurate, and the focal length of a zoom lens may be hard to estimate. Second, we do not generally work from a 1:1 positive, but instead either read distances on a photographic enlargement or count picture elements (pixels) on a television screen. In doing so we will have altered the apparent focal length of the image by an unknown amount. We can solve for the "magnified" focal length analytically using

$$f'_c = \frac{x_e}{\tan(\delta/2)} \tag{15}$$

where x_e is the measured distance from the principal point to the right-hand edge of the enlarged image and δ is the horizontal field of view of the lens. Unfortunately, for most cases, δ itself is not accurately known. Third, the direction of aim of a camera in the field is generally chosen to give the best view. Thus the ground coordinate system defined by the principal line may not be particularly convenient. The transformed ground points can be easily rotated into a more traditional coordinate system, for example with the x axis directed offshore, if the angle ϕ between the two coordinate systems is known. Unfortunately, accurate estimation of ϕ in the field is again difficult.

The unknowns f'_c, τ, and ϕ can be determined quite accurately by making use of targets at known locations in the image. By knowing both the ground and image coordinates of particular points, (12), (13), and (14) can be solved iteratively to calculate the unknowns. If one known point and the horizon are used, the solution will be unique. If two or more known points are used, the problem is overdetermined and can be solved by minimizing an appropriate error term. Using this technique in analyzing the images discussed later in the paper, we find typical errors in the estimates of τ, ϕ, and f'_c to be less than 0.25°, 0.5°, and 0.5%, respectively, roughly consistent with theoretical expectations discussed below.

Theoretical Resolution and Accuracy

The photogrammetric measurements outlined in the last section are based on estimates of one distance (the camera height) and two angles (vertical and azimuthal). The precision of the technique then relies on the precision of each of these estimates.

While there may be errors associated with estimating camera height above some surface, there is no inherent limitation on that measurement. On the contrary, there is a discrete resolution associated with our estimates of angle. For image quantification we use an image processing system (described later) which breaks the image into a 512 × 512 array of pixels. Since we can resolve to no better than ± 1/2 pixel, we find a fundamental limit on angular resolution to be $\Delta\alpha = \Delta\gamma = \delta/1024$ (assuming $\tan\delta/2 \approx \delta/2$). For our typical wide-angle lens, $\delta = 40°$, so $\Delta\alpha = 0.04° = 7 \times 10^{-4}$ radians.

From (12) we see that the precision of estimates in Y_Q is given by

$$\frac{\Delta Y_Q}{Y_Q} = \frac{\Delta H_c}{H_c} + \frac{2\Delta(\tau + \alpha)}{\sin 2(\tau + \alpha)}$$

$$\approx \frac{2\Delta(\tau + \alpha)}{\sin 2(\tau + \alpha)} \approx \frac{1.4 \times 10^{-3}}{\sin 2(\tau + \alpha)} \tag{16}$$

Sensibly, resolution degrades as $(\tau + \alpha)$ approaches $\pi/2$, or as the point of view approaches the horizon. If we take the maximum useful vertical angle to be 85° (5° from the horizon), the resolution in Y will be 0.8%. Note that the fractional errors also increase as the view approaches nadir. However, this is simply a result of normalizing by Y_Q, which goes to zero at the nadir; absolute errors will actually be a minimum.

The error in X estimates (normalized by Y_Q, roughly representing the distance from the camera) is given by

$$\frac{\Delta X_Q}{Y_Q} = \left(\frac{\Delta H_c}{H_c}\right)\frac{\tan\gamma}{\sin(\tau + \alpha)} + \frac{\tan\gamma\,\Delta(\tau + \alpha)}{\cos(\tau + \alpha)}$$

$$+ \frac{1}{\sin(\tau + \alpha)}\frac{\Delta\gamma}{\cos^2\gamma} \tag{17}$$

For typical camera views, $\sin(\tau + \alpha) \approx 1$; hence the theoretical resolution is again limited by angular resolution through the last two terms. Using representative values, we find a worst case resolution of 0.3%, a smaller value than for Y, partly due to the choice of normalization. Since the camera coordinate system is not usually aligned with the survey system, we chose a conservative estimate that spatial

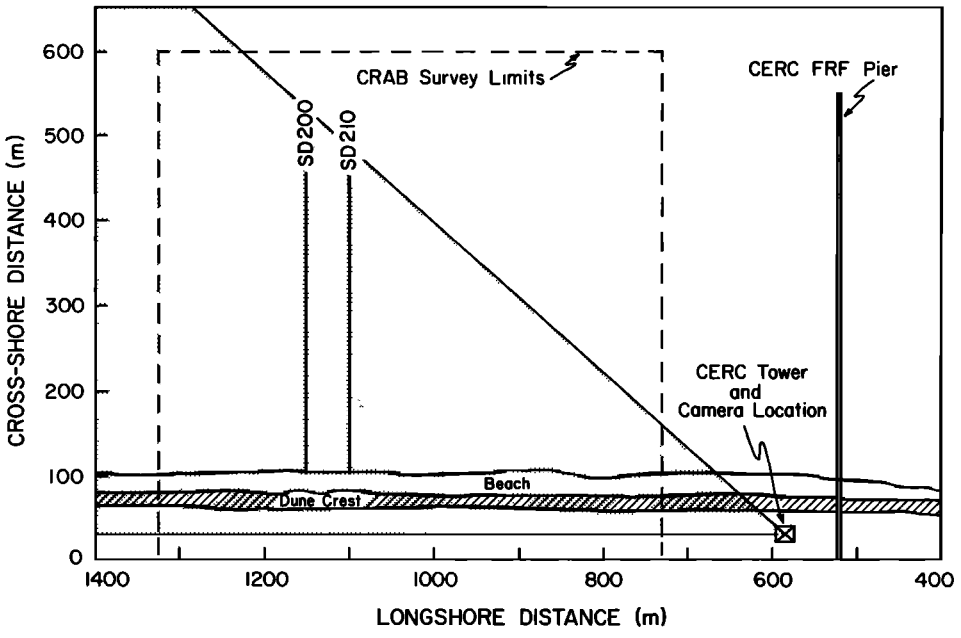

Fig. 8. Map of the field site during the October portion of SUPERDUCK. The stippled area indicates the ground coverage in the field of view of the camera. Cross-shore transect SD200 is the location of some example profiles in the text, while SD210 is the location closest to the main instrument line in SUPERDUCK. Longshore spacing for the CRAB survey lines was 20 m (there exists an intermediate line, SD205, between the two lines indicated).

resolution in either axis will be of the order of 0.8% of the distance from the camera.

While fundamental limits on precision depend, for our system, simply on the angular size of the pixels, the absolute accuracy of our measurement depends on cumulative errors from a number of estimates. If the location of the camera is well known, the error in the first term of (16) and (17) results largely from errors in determining sea level (assuming that the ocean surface is being imaged). For the data discussed later, this will be of the order ± 0.25 m with a camera height of 40 m, so that the relative error contribution is 0.65%. This error could be substantially larger for lower camera heights. Estimation of the vertical and horizontal angles actually incorporates parameters such as τ, f, and ϕ, each of which has associated errors. If we assume that the parameters themselves were estimated based on the location of two known points (as outlined in the previous discussion), then they will collectively incorporate the error of four separate angle measures, $4\Delta\alpha$. Including the error associated with estimating the angle of interest, the total angular error could be $5\Delta\alpha = 0.20° = 3.5 \times 10^{-3}$ radians. For a maximum vertical angle of 85°, and including the error for camera height, the theoretical worst case accuracy should be

$$\frac{\Delta X_Q}{Y_Q} < \frac{\Delta Y_Q}{Y_Q} \approx 0.65\% + (5 \times 0.8\%) < 5\% \qquad (18)$$

As shown, the accuracy and resolution of the system depends on the angular field of view δ and the vertical angle $(\tau + \alpha)$. The value of δ used here is for a wide-angle lens and gives a worst case result. Clearly, a telephoto lens, zoomed in on the subject at hand, will yield improved estimates. The vertical angle becomes critical as $(\tau + \alpha)$ approaches the horizon. While 85° is a reasonable value for a maximum angle, a better approach to experimental design would be to determine the required resolution and camera geometry, then solve for the maximum vertical angle for which this resolution is achievable.

Field Techniques

The time exposure technique for estimating the incident wave dissipation distribution and hence large-scale nearshore morphology was tested as part of the DUCK85 and SUPERDUCK experiments in September 1985 and October 1986, respectively, at the Army Corps of Engineers Field Research Facility (FRF) in Duck, North Carolina. The DUCK85 experiment [*Mason et al.*, 1987] was used to perform initial testing primarily with standard 35-mm cameras and simple photographic time exposure techniques. The images acquired were projected onto an x-y digitizer table, and the location of the intensity maximum determined visually [*Holman and Lippmann*, 1987]. Results from that experiment were encouraging but indicated a need for further quantification and for more sophisticated digitization methods.

During SUPERDUCK the use of video imagery was implemented as an improvement to the photographic technique. A Panasonic black-and-white television camera was mounted on top of a 40-m-high tower erected on the dune crest. Figure 8 is a map of the field site during the October portion of the SUPERDUCK experiment showing the location of the study area, referred to as the minigrid, in relation to the FRF tower and the ground coverage associated with the camera.

Hourly video records of 20-min length were acquired from October 6–16. Time exposures were created digitally by mathematically averaging successive video frames over a 10-min period using an Imaging Technology image processing system in a DEC LSI 11/73 host computer (Figure 1*b* is an example time exposure image from October 10). Using the photogrammetry results, the time exposure image can be rectified to produce a map view with known scaling. The rectification process involves mapping the oblique image

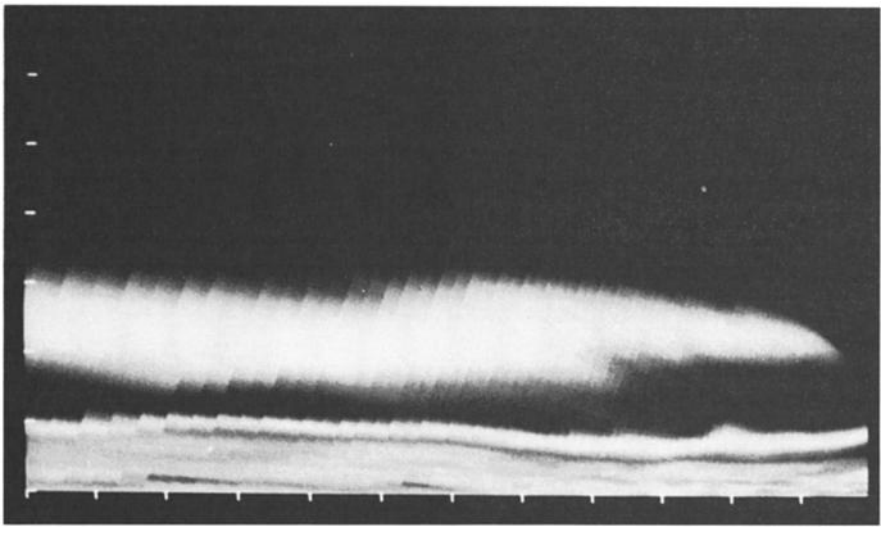

Fig. 9. Rectified time exposure image obtained at low tide on October 16, 1986, encompassing the minigrid area. The longshore and cross-shore distances are scaled equally with tic mark spacing of 50 m. The thin white band indicates the shore break, while the broader offshore band shows breaking over the bar. The relative size in raster width reflects the pixel resolution in the original time exposure.

intensities, pixel by pixel, onto the scaled grid. From the rectified view, cross-shore intensity profiles at prescribed longshore distances are easily found. Figure 9 is the rectified image of the minigrid area outlined in Figure 1*b*. Figure 10 shows an example cross-shore intensity profile and the local bathymetry. Clearly, there are local maxima in the intensity distribution in the vicinity of the shoreline and the bar, which appear very similar to the model results presented earlier (Figure 4). Note that only relative magnitudes of intensity are relevant within an image; absolute magnitudes vary with ambient light and camera aperature.

Quantification of images is accomplished using an image processing system. Extracting information with this system is objective and allows for minimum handling of raw data. Furthermore, with the aid of the image processor we may digitally enhance the images to best reveal the information available. For example, though some video records do not yield high-contrast raw images, the image processor allows us to increase the dynamic range of the image by stretching the contrast to as many as 256 gray shades.

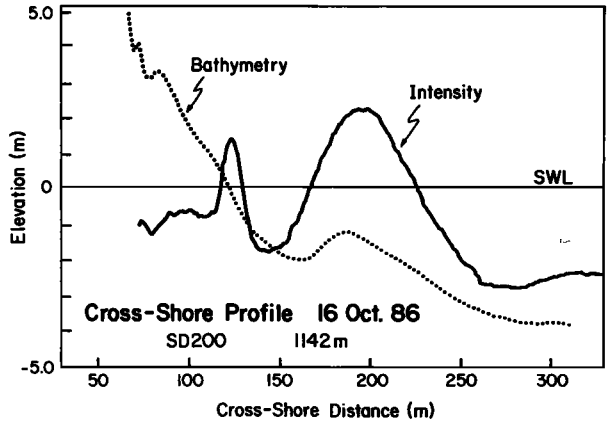

Fig. 10. Example cross-shore intensity profile and bathymetry for October 16, 1986, during SUPERDUCK. The intensity values are nondimensional with absolute magnitudes that are not related to the bathymetry.

Ground truth bathymetry data during SUPERDUCK were collected by the FRF staff using the CERC Coastal Research Amphibious Buggy, or CRAB [*Birkemeier and Mason*, 1984]. Figure 8 shows the location of the intensive survey region referred to as the minigrid. The bathymetry was sampled once per day (October 6, 9–16) along preset cross-shore profile lines spaced approximately 20 m apart alongshore. Each survey went beyond the first (and most prominent) sand bar, with the exception of the tenth, when adverse conditions prevented survey completion. Figure 11 shows three-dimensional oblique views of the minigrid survey for October 6, 9, 11, 13, 15, and 16 [*Birkemeier et al.*, 1988].

A maximum of 20 shore-normal image intensity profiles within the minigrid area were analyzed for each data run. As in Figure 10, each profile contained a maximum intensity (or peak) in the vicinity of the shoreline and the bar, provided the waves were breaking offshore. Given the large amount of data, 464 cross-shore comparisons, not all the profile plots are included. Instead most of the data are summarized in the following analysis using two-dimensional plan view maps indicating the surveyed bar location and digitized intensity maximum location at different stages of the tide. With this sampling scheme we are able to determine the behavior of the cross-shore intensity distribution in relation to the bathymetry under varying wave conditions, water levels, and beach state. Table 1 summarizes the sampling times, wave conditions, and video quality for each data run.

Results

Time Exposures

The research objectives of the time exposure technique are threefold. The first is to infer the presence of a sand bar from an offshore intensity maximum corresponding to the maximum time-averaged incident wave dissipation. The

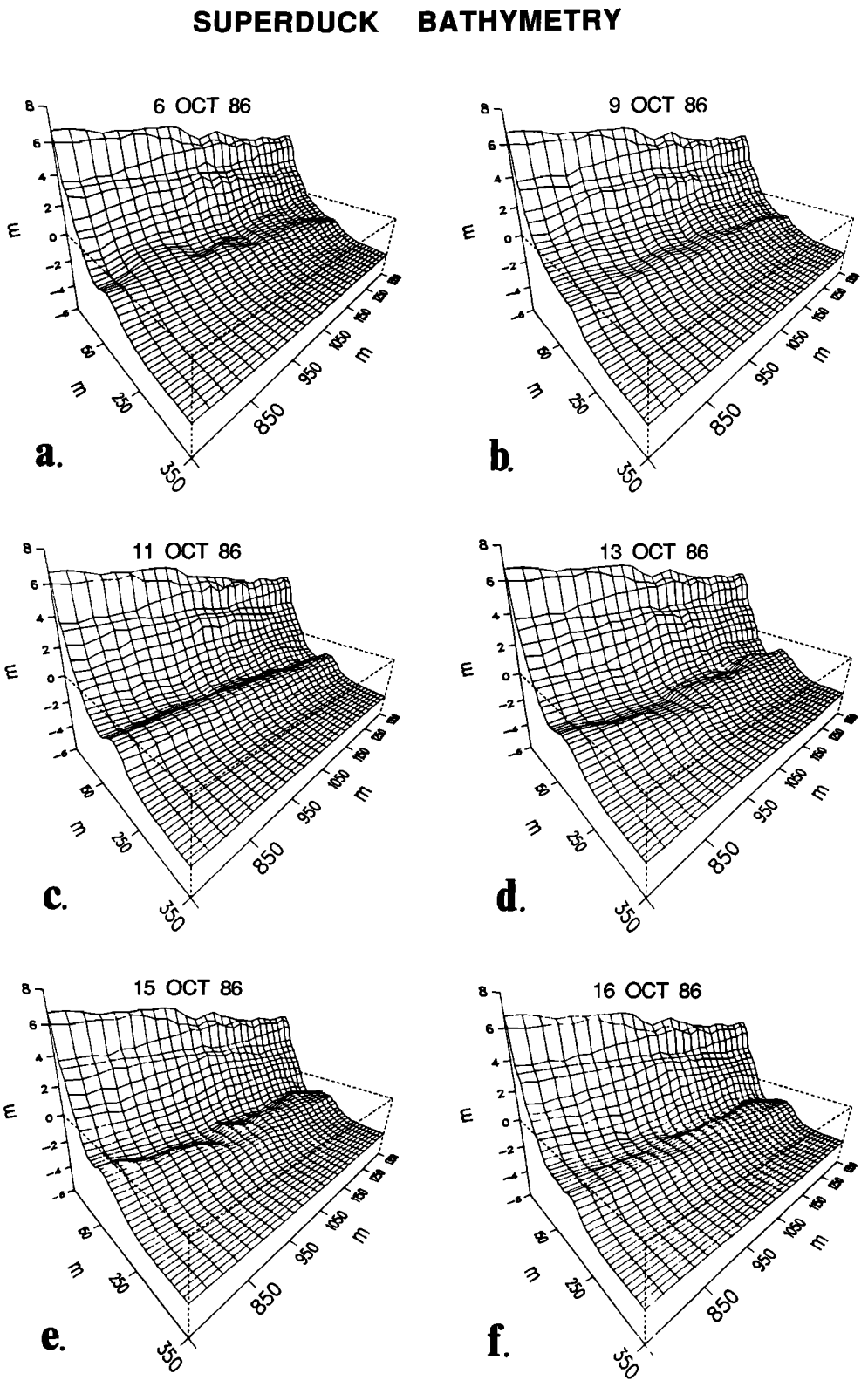

Fig. 11. Three-dimensional oblique views of the minigrid survey during SUPERDUCK [*Birkemeier et al.*, 1988].

second is to determine the cross-shore length scale of the bar from the location of the intensity maximum. The third is to detect the presence of any longshore variability in the bar and determine appropriate longshore length scales. We will examine each objective in turn.

The theoretical dissipation model suggests that best results will be obtained for small waves that just break over the bar (H_c^* values of 0.5 to 1.0). For October 6 an average value of H_c^* was approximately 0.85, and while the bathymetry was complex, there were local regions of good

TABLE 1. Sampling Time, Wave Conditions and Video Quality for Morphology Images Discussed in Text

Date (October)	Tide, m	Time, EST	H_{rms}, m	f, Hz	Video Quality
6	low −0.11	1400	0.82	0.1680	good
6	mid 0.25	1730	0.56	0.1719	good
9	high 0.80	1130	0.43	0.1641	good
9	mid 0.27	1445	0.44	0.1641	good
9	low −0.27	1800	0.38	0.1641	good
10	low −0.08	0600	0.33	0.2656	good
10	mid 0.55	0915	1.35	0.1484	poor (rain)
10	high 1.10	1230	1.58	0.1406	poor (rain)
11	low 0.09	0720	2.06	0.1094	good
11	mid 0.56	1040	2.13	0.1563	good
11	high 1.06	1400	2.06	0.1016	good
12	low 0.03	0830	1.65	0.0938	excellent
12	mid 0.45	1145	1.85	0.0859	excellent
12	high 0.93	1500	1.77	0.0859	excellent
13	low −0.22	1000	1.20	0.0820	good
13	mid 0.15	1230	1.25	0.0977	good
13	high 0.73	1600	1.25	0.0977	good
14	low −0.36	1100	0.75	0.0977	poor (noisy)
14	mid 0.17	1400	0.69	0.1055	poor (noisy)
14	high 0.70	1700	0.61	0.0938	poor (noisy)
15	low −0.22	1130	0.77	0.1719	good
15	mid 0.30	1445	0.64	0.1719	good
15	high 0.76	1800	0.54	0.1641	good
16	high 0.91	0600	0.49	0.2349	good
16	mid 0.40	0915	0.68	0.1992	good
16	low −0.30	1230	0.72	0.2031	good

bar definition (Figure 11*a*). Figure 12 shows the midtide intensity transects for the three best defined sand bar profiles (determined from minigrid bathymetry). The intensity maxima clearly indicate the presence of the sand bar, although the peak definition is somewhat subtle for the y = 1187 transect, consistent with the subtle nature of the bar. There is excellent agreement between the locations of the intensity maxima and bar crest, well within the resolution of the image. This supports the validity of the model and the potential of the technique for imaging morphology under optimal conditions.

Figure 13 is the rectified time exposure image obtained at low tide on October 11, a day when model performance was expected to be poorer due to the larger wave heights (average $H_c^* \approx$ 4.3, 2.6, and 2.4 for low, middle and high tide, respectively). The bathymetric survey (Figure 11*c*) showed the bar to be linear with no longshore variability. The intensity distribution in Figure 13 confirms this, showing a clearly linear pattern and providing a good qualitative description of the sand bar.

While the qualitative description is good, the quantitative behavior of the technique breaks down in an unexpected way. Figure 14 shows the location of the intensity peak for low, middle, and high tide over the minigrid area. Also shown are the locations of the mean shoreline and bar crest. The latter is depicted by a central line (the best estimate of bar crest position) surrounded by a stippled area, reflecting the fact that the bar itself may not be well defined. (From Figures 12 and 17, it is clear that bar definition is typically based on three CRAB survey points with a typical spacing of 15 m and whose locations are subject to operator subjectivity. To parameterize this uncertainty, we have added the stippled area whose bounds correspond to a deepening by 5% of the bar crest depth h_c, usually 5–10 cm.)

The shape and trend of the bar in Figure 14 appears to be preserved at all stages of the tide. However, the offshore location of the intensity peaks does not fall over the bar, and in fact lies inside the crest well into the trough. This result cannot be reproduced in any way by our model and shows that our assumption that the average visual wave breaking signal represents incident wave dissipation is invalid under these conditions.

Investigation of the original video images reveals two apparent sources for the error. The finite distance required for wave reformation after passing the bar crest appears to provide a minor landward offset. Most of the error appears to stem from preferential persistence of foam in the trough

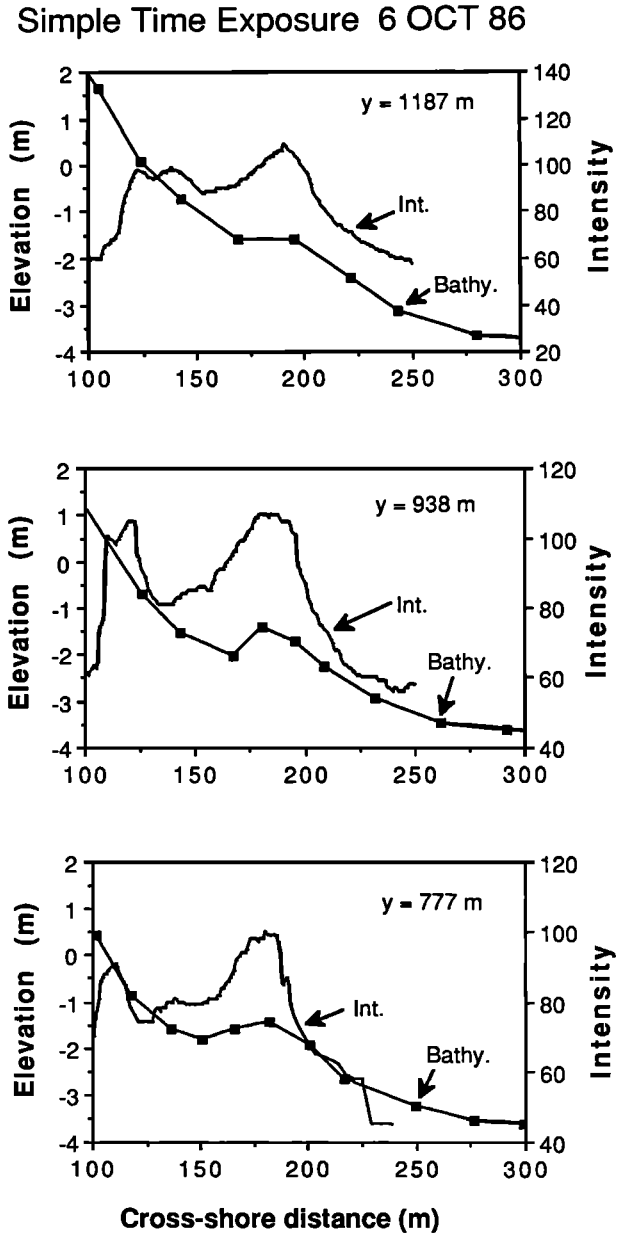

Fig. 12. Local bathymetry and cross-shore intensity profiles from a simple time exposure obtained at midtide on October 6, 1986. The three transects were chosen as having the best defined bars.

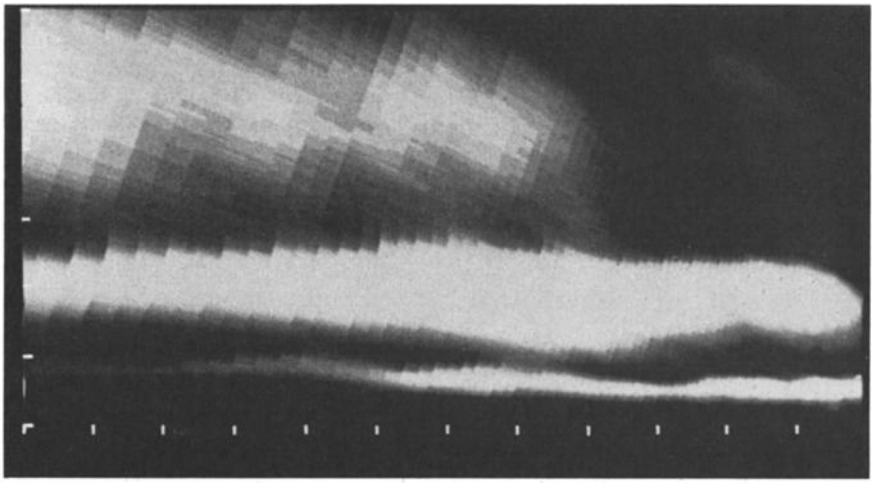

Fig. 13. Rectified time exposure image encompassing the minigrid area obtained at low tide on October 11, 1986. The longshore and cross-shore distances are scaled equally with tic mark spacing of 50 m. The image contrast has been stretched to better reveal the bar location. The weak offshore intensity maximum corresponds to a poorly defined second bar.

region. This differential in foam persistence weights the intensity maximum shoreward from the location of maximum wave dissipation. We know of no testable physics to describe this behavior and hence allow us to remove the bias. By examining those records for which a well-defined bar is present, we find that approximately 42% of the intensity maxima were located shoreward of bar crest and that these were generally associated with high waves and strong onshore winds. This latter observation suggests a potential mechanism which would need considerable further testing, though it should be noted that moderate-to-strong onshore winds could blow spray from the active wave breaking regions (especially for plunging breakers) shoreward to cause an inshore bias in the maximum intensity location. In addition, high winds could cause whitecaps in regions of little or no incident wave breaking, also biasing the intensity distribution.

The capabilities of the technique for detecting and quantifying longshore variability are illustrated in Figure 15, a comparison of shore-parallel transects of intensity and bathymetry for October 16, a day of lower waves ($H_c^* \approx 1.7$). The two transects differ by 10 m in offshore location and are centered about the mean bar position. The intensity and bathymetry profiles for this day and for all others tested from SUPERDUCK showed similar structure. The presence of

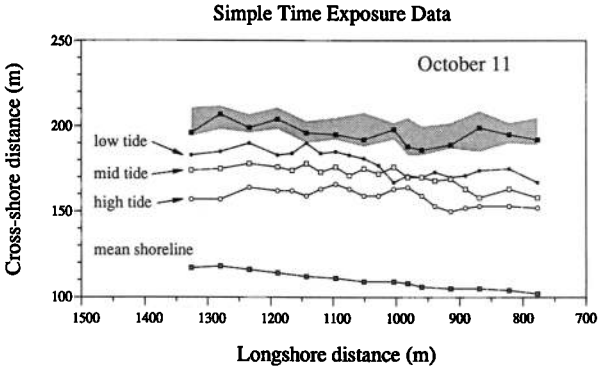

Fig. 14. Location of the mean shoreline, measured bar crest (solid squares), and intensity maxima from simple time exposures obtained at low, middle, and high tide on October 11, 1986. The stippled area indicates the area around the crest for which the water depth is within 5% of h_c.

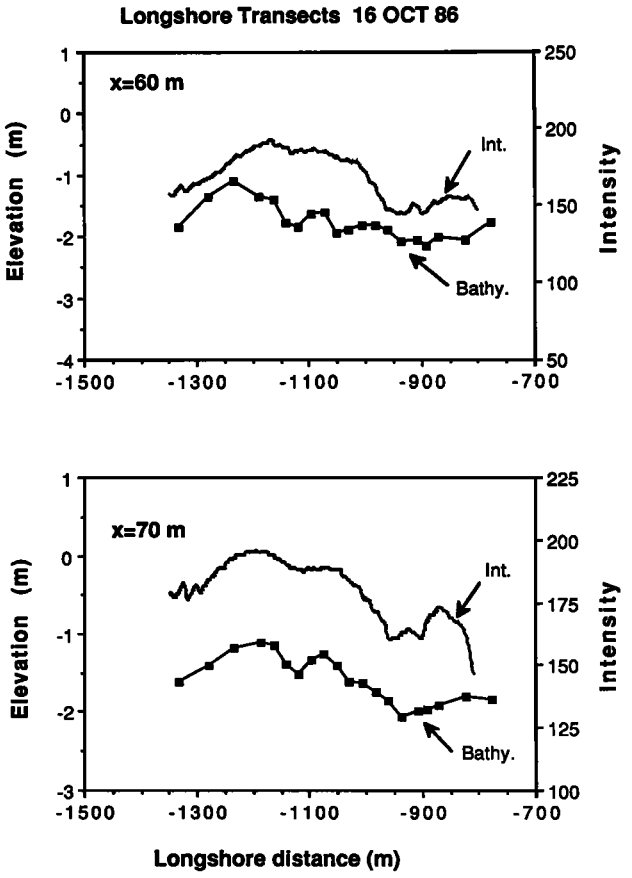

Fig. 15. Shore-parallel transects centered over the mean bar distance, 60 m (upper panel) and 70 m (lower panel) offshore, from a simple time exposure obtained at low tide on October 16, 1986. Variations of intensity correspond to the underlying bathymetry.

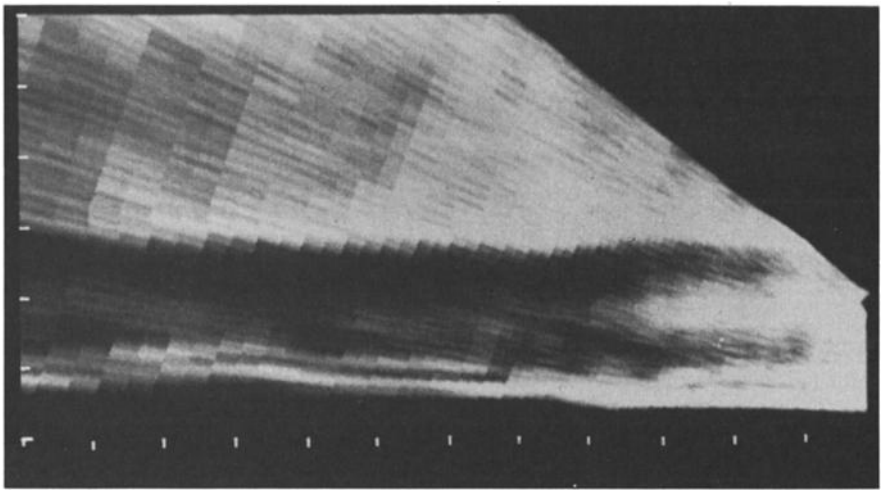

Fig. 16. Rectified differencing time exposure obtained at low tide on October 12, 1986. The bright white band offshore indicates the presence of a sand bar, whereas the shoreline is indicated by a relative darkness within the shorebreak region. The longshore and cross-shore distances are scaled equally with tic mark spacing of 50 m.

dips in the shore-parallel bathymetry (caused possibly by topographically trapped rip currents), originally a concern, does not appear to cause a problem, since the relative "darkness" above the deeper channel is imaged in a consistent manner with the darkness due to reduced breaking in the same region. Several other examples of rhythmic morphology from other times of year confirm the robustness of the technique for this purpose, indicating that the time exposures can in fact be used to detect and measure dominant longshore length scales of a sand bar system [*Holman and Sallenger*, 1986].

Overall, the time exposure technique appears to be a very useful tool for determining the presence of a bar system as well as the presence and length scales of longshore variability. Cross-shore scales are well reproduced under certain conditions, but an observer hoping to use photographic time exposures, for example, would have to bear in mind the potential foam bias and make a qualitative assessment of the problem before quantifying any sample (residual foam is visible, so at least an assessment can be made). This problem seems to reduce the effectiveness of the time exposures. However, if an image processing system is available, more powerful techniques are available to improve the situation. We have developed a modification to the technique, called differencing time exposure, that eliminates this problem.

Differencing Time Exposures

One way to altogether avoid the dynamics of residual foam accumulation is to eliminate unwanted, persistent signals that do not pertain to active breaking (thus energy dissipation). This elimination can be accomplished by subtracting video frames, separated in time by a given interval (commonly 0.5–1.0 s) to yield a difference image. Regions of little or no contrast change, such as areas of persistent foam, will show zero difference. Areas of active breaking will show large intensity changes, hence large difference signals. A time exposure can be made by averaging a set of these difference images over a suitable period, again 10 min for our case. Figure 16 is an example rectified differencing time exposure image from October 12. The offshore breaking pattern is indicated again by the high-intensity band offshore.

The differencing technique requires the selection of two free parameters to yield an optimal image. The first is the time interval between images to be subtracted. The second is a threshold value below which contrast differences are considered negligible (and are mapped to zero). This threshold serves the double purpose of eliminating minor values of difference that result from camera shake or the inevitable video noise, as well as eliminating the negative values of difference (since time averaging allowing both positive and negative differences must always be zero). While resulting image quality is influenced by the particular values of these parameters, the conclusions about sand bar morphology (intensity peak locations) are not overly sensitive. Fixed values have been used throughout this paper to eliminate selective bias.

We start our examination of the differencing time exposure technique by again looking at the limiting case where waves just begin to break over well-defined bar crests. Figure 17 is a bar location map for October 9 indicating the estimated bar location and intensity maxima at low ($H_c^* \approx$

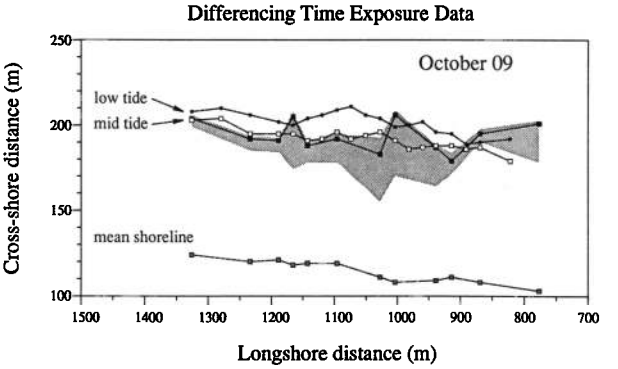

Fig. 17. Location of mean shoreline, measured bar crest (solid squares), and intensity maxima from differenced time exposures obtained at low and midtide on October 9, 1986. The stippled area indicates the area around the crest for which the water depth is within 5% of h_c.

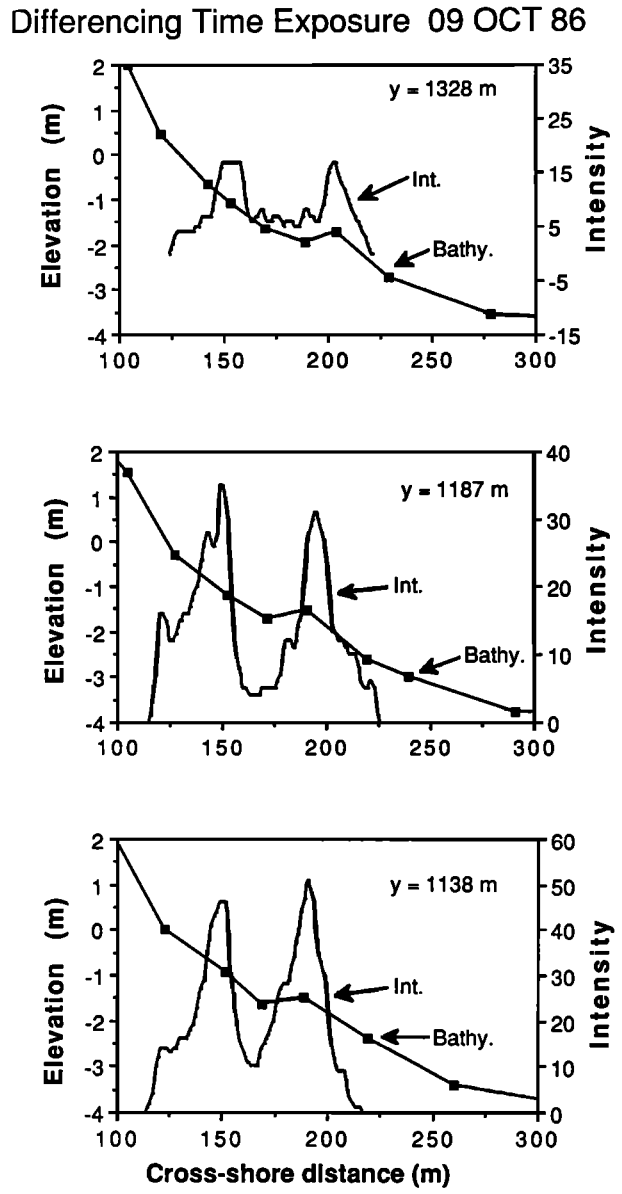

Fig. 18. Local bathymetry and cross-shore intensity profiles from a differenced time exposure obtained at midtide on October 9, 1986, for the three best defined sand bar locations.

0.8) and midtide ($H_c^* \approx 0.6$) for the differencing algorithm ($H_c^* \approx 0.45$ at high tide and no waves were breaking offshore). At midtide the intensity maximum location falls within the survey error of the position of the bar crest, indicating a good estimate at all longshore locations. Cross-shore profiles corresponding to several regions with well-defined bar crests are shown in Figure 18. Not surprisingly the offshore intensity maximum shows excellent agreement with the bar crest location. Furthermore, the intensity maximum has moved offshore at lower water level, consistent with the results of the dissipation model (Figure 6; equation (10)).

Figure 19 shows the results of the differencing technique for October 11, when the bar was linear but the simple time exposure results were their worst. The improvement is immediately evident; at high tide ($H_c^* \approx 2.4$) the intensity locations lie quite near the crest within the range of bar

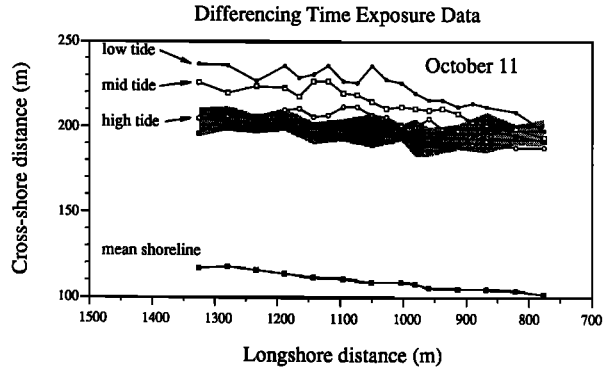

Fig. 19. Location of mean shoreline, measured bar crest (solid squares), and intensity maxima from differenced time exposures obtained at low, middle, and high tide on October 11, 1986. The stippled area indicates the area around the crest for which the water depth is within 5% of h_c.

estimate for most of the data. At lower tide levels the intensity moved offshore, consistent with greater dissipation offshore. For low tide ($H_c^* \approx 4.3$) the mean value of $\Delta x/x_c \approx$ 39%, somewhat above the same range for the model calculations (Figure 6) but not unreasonable.

Figure 20 shows the performance of the technique for October 16 when the bathymetry was quite variable in the longshore. At high tide ($H_c^* \approx 0.4$) the waves were barely breaking over the bar, and the intensity maximum provided an excellent mapping of even this complicated bar morphology. However, for low tide ($H_c^* \approx 1.7$), the differencing time exposure maximum is further offshore and corresponds to the location of the more continuous slope break at about 1.75-m depth. The H_c^* value for the slope break was approximately 1.0, large enough to allow significant breaking there. This may explain the "selection" by the technique of the straighter slope break instead of the complicated and more poorly defined bar crest.

The above discussion supports the hypothesis that our time exposure technique (modified by a differencing algorithm) is representative of energy dissipation of incident wave breaking. Continuing the comparison, we attempt to characterize the discrepancies in bar location Δx as a func-

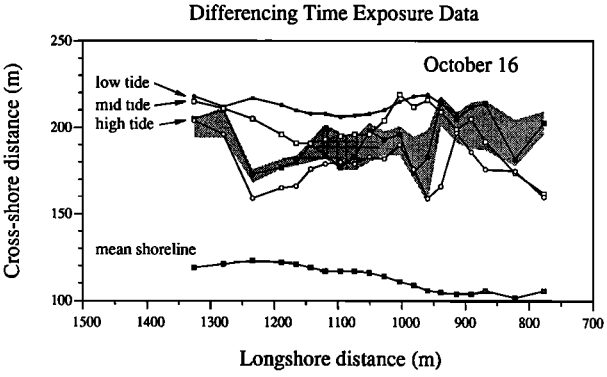

Fig. 20. Location of mean shoreline, measured bar crest, and intensity maxima from differenced time exposures obtained at low, middle, and high tide on October 16, 1986. The stippled area indicates the area around the crest for which the water depth is within 5% of h_c.

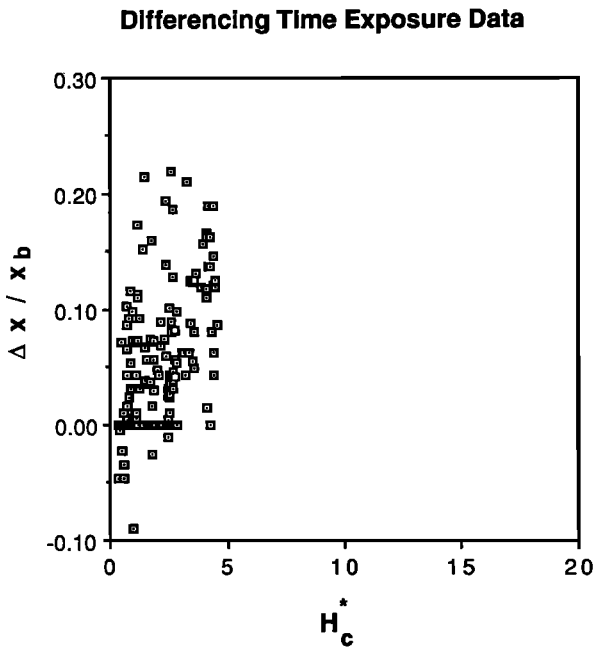

Fig. 21. Results from differencing time exposures on October 9, 11–13, 15–16, showing the fractional error in locating the bar crest plotted against nondimensional wave height H_c^*. Negative $\Delta x/x_{bar}$ values indicate a landward offset in intensity bar location estimate.

tion of nondimensional wave height H_c^*. The Δx values arising in the differencing technique for October 9, 11–13, 15–16 are normalized by the mean distance to the bar crest (different along each profile for each day) and plotted against H_c^* in Figure 21. The results, while noisy, are not inconsistent with the model behavior shown in Figure 6.

Shoreline Agreement

A further feature in time exposures is the representation of a shore break which shows up as higher intensity values along the beach face. The cross-shore profiles shown in Figures 12 and 18 have well-defined peaks in the vicinity of the shoreline. This intensity maxima for all cross-shore profiles (from simple time exposures) are compared quantitatively with the calculated shoreline location in Figure 22. The calculated shoreline location was determined as the intersection of the linearly interpolated profile and the still water level at the time of the survey. The correlation is very good (r = 0.92); however, the slope of the line through the data is slightly greater than unity, potentially a result of setup or other swash dynamics. For individual days the agreement is excellent; for example, on October 12 when image quality was best the intercept is –2.0 and the slope 1.02 (r = 0.97).

The persistence of foam near the mean run-up location generates an unusual result for the differencing technique. Since foam intensity appears fairly constant, the contrast difference will always be low; hence the mean shoreline for the differencing image often shows an intensity minimum that corresponds to the location of the maximum for the simple time exposure. Shoreline location appears best done with the simple time exposure.

Discussion

Both the simple time exposure and the differencing time exposure techniques seem to provide a valuable tool for studying nearshore morphology. Both detect the presence of a bar system and allow measurement of any dominant longshore length scales of rhythmicity. Both can be used to estimate cross-shore length scales, a necessary prerequisite for testing bar generation models. The results from the differencing technique are quite similar to the model, which is based on sound physics, so relative errors are better understood and, fortunately, are constrained by incident wave saturation. The simple time exposure technique may be biased by problems associated with residual foam accumulation, so that for nondimensional wave heights H_c^* greater than about 1, estimates of bar position can be subject to error for which we have little understanding. Nonetheless, our results show that the simple time exposure will generally yield good bar position estimates. This is due to a fortuitous case of compensating errors; dissipation of larger waves tends to give errors in the offshore direction, while foam tends to compensate toward the onshore. Unfortunately, we have only a qualitative understanding of the process. When residual foam is apparent, the technique will work best at low tide when H_c^* is low, and will generally be worse for higher tides (higher H_c^*). Correcting the offshore discrepancy between intensity maximum and bar crest locations using H_c^* would be difficult; details in the beach profile, as well as surface foam biasing, may cause errors in the location of intensity maxima which are unrelated or not easily related to the H_c^* parameter. Thus, we stop short of calculating correction equations for the bias.

The relevance of H_c^* in understanding errors in the technique is reassuring from a theoretical point of view. However, it is of dubious practical value, since we do not know h_c, the depth at the bar crest. Instead, a user of the

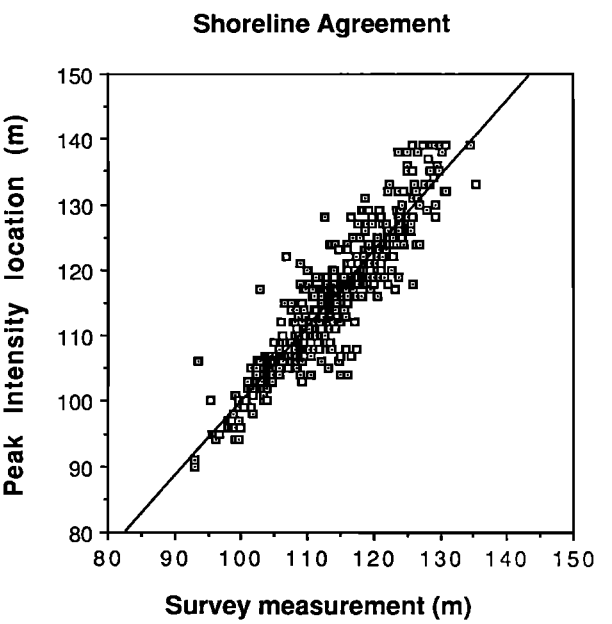

Fig. 22. All shoreline intensity maxima locations from simple time exposures obtained at low, middle, and high tide on October 6, 9–16, plotted against measured shoreline location. The regression line is given by $y = -14.8 + 1.15x$ (r = 0.92).

technique must refer back to the qualitative wave parameterizations. Both simple and differencing techniques work well when the waves are "just breaking" over the bar. The simple technique starts to break down when the presence of foam no longer seems directly related to the amount of local dissipation. Both of these limits are of a type that may be visually assessed prior to analysis.

The calibration of the time exposure technique discussed in this paper assumes that the appropriate measure of a sand bar location is the point of minimum depth. This may not always be true. For example, for the bar generation mechanism presented by *Holman and Bowen* [1982] the sand bar is treated as a perturbation to an underlying beach profile. The point of maximum perturbation will always be offshore from the point of minimum depth, on the seaward slope of the typical bar where the local slope equals a representative mean slope. Thus the errors in the time exposure technique will probably be less for this application. Holman and Bowen also point out that in their theory a low-tide terrace can be thought of as a small-amplitude bar. Again, the appropriate location of the maximum perturbation would be at the slope break, just the point imaged by the time exposure technique.

CONCLUSIONS

We have developed a technique to measure the scales and morphology of natural sand bars based on the preferential dissipation of wind waves and swell over the shallows of the bar. We do not actually measure dissipation, but instead record the visual signal created by breaking incident waves and assume that this is proportional to dissipation. The visual wave breaking patterns are imaged photographically, with statistical uncertainty reduced by the use of time exposures (essentially averaging over a length of time long compared with modulation time scales for incident wave height). Analysis of the photogrammetry shows that positional information in the resulting images can be quantified to an accuracy of 5% of the distance to the camera.

Theoretical modeling shows the sensitivity of incident wave dissipation to perturbations in bottom slope; hence the potential for using dissipation to locate bars. An important parameter is the nondimensional wave height $H_c^* = (H_0/\gamma h_c)(k_c/2k_0)^{1/2}$, where H_0 is the deep-water RMS wave height, h_c and k_c are the depth and wave number at the bar crest, k_0 is the deep-water wave number, and γ is a breaker constant, taken as 0.42 for this study. For $H_c^* = 0.5$–1.0 the waves are just breaking and the dissipation maximum corresponds well to the bar crest position. Larger H_c^* result in weighting the dissipation maximum farther offshore up to a maximum location beyond which the local wave field is saturated. The maximum discrepancies based on a reasonable example are 35% of the true bar crest distance.

Ground truth testing, conducted during SUPERDUCK, confirms the capabilities of the time exposure technique for detecting the presence of a sand bar system as well as detecting longshore variability and rhythmicity and quantifying length scales. Cross-shore scale estimates are good for small H_c^*, but for higher waves, persistent foam biases the intensity shoreward in ways for which we have no theory. The use of video differencing (the subtraction of consecutive frames) removes residual foam from the image, and results from differencing time exposures appear consistent with our theoretical dissipation modeling. Relative errors may be assessed using H_c^*, but adjustment corrections may not be reliably made using this parameter due to unknown profile characteristics and a breakdown in understanding the physical behavior of surface foam accumulation.

Acknowledgments. We would like to thank the entire FRF staff for their tireless efforts during SUPERDUCK, particularly Curt Mason (who made it all happen), Bill Birkemeier, and Ronbo. COL Grum was instrumental in approval and construction of the FRF tower. Much credit and personal thanks are owed to Paul O'Neill, whose engineering skills and programming contributions made this work possible. Funding for the development of the image processing system and time exposure technique was provided by the Office of Naval Research, Coastal Sciences Program, under contract N00014-84-0218. The ground truth study during SUPERDUCK was funded by the U.S. Army Corps of Engineers, Coastal Engineering Research Center under the Barrier Island Sedimentation work unit (thanks, Suzette). The analysis was carried out while the authors were on temporary leave at Dalhousie University, and we thank them for their hospitality. Finally, thanks to Marcia for the care packages.

REFERENCES

Battjes, J. A., Set-up due to irregular waves, Proceedings of the 13th International Conference on Coastal Engineering, pp. 1993–2004, Am. Soc. Civ. Eng., New York, 1972.

Battjes, J. A., and J. P. F. M. Janssen, Energy loss and set-up due to breaking of random waves, Proceedings of the 16th International Conference on Coastal Engineering, p. 569, Am. Soc. Civ. Eng., New York, 1978.

Birkemeier, W. A., and C. Mason, The CRAB: A unique nearshore surveying vehicle, *J. Surv. Eng.*, *110*(1), 1–7, 1978.

Birkemeier, W. A, C. F. Baron, M. W. Leffler, H. C. Miller, J. B. Strider, and K. K. Hathaway, SUPERDUCK nearshore processes experiment: Data summary, miscellaneous reports, Coastal Egn. Res. Cent., Field Res. Facil., U.S. Army Eng. Waterw. Exp. Sta., Vicksburg, Miss., 1988.

Bowen, A. J., Simple models of nearshore sedimentation: Beach profiles and longshore bars, Coastline of Canada, Littoral Processes and Shore Morphology, *Geol. Surv. Pap.*, *80–10*, 1–11, 1980.

Bowen, A. J., and D. L. Inman, Edge waves and crescentic bars, *J. Geophys. Res.*, *76*, 8662–8671, 1971.

Carter, T. G., P. L. Liu, and C. C. Mei, Mass transport by waves and offshore sand bedforms, *J. Waterw. Harbors Coastal Eng. Div. Am. Soc. of Civ. Eng.*, *WW2*, 165–184, 1973.

Collins, J. I., Probabilities of breaking wave characteristics, Proceedings of the 13th International Conference on Coastal Engineering, pp. 399–412, Am. Soc. Civ. Eng., New York, 1970.

Crowson, R. A., W. A. Birkemeier, H. M. Klein, and H. C. Miller, SUPERDUCK nearshore processes experiment: Summary of studies, technical report, Coastal Eng. Res. Center., Field Res. Facil., U.S. Army Eng. Waterw. Exp. Sta., Vicksburg, Miss., 1988.

Galvin, C. J., Jr., and P. S. Eagleson, Experimental study of longshore currents on a plane beach, *Tech. Memo. 10*, U.S. Army Coastal Eng. Res. Cent., Fort Belvoir, Va., 1965.

Goda, Y., Irregular wave deformation in the surf zone, *Coast. Eng. Jpn.*, *18*, 13–26, 1975.

Harris, W. D., and M. J. Umbach, Underwater mapping, *Photogramm. Eng.*, *34*, 765–772, 1972.

Holman, R. A., and A. J. Bowen, Bars, bumps, and holes: Models for the generation of complex beach topography, *J. Geophys. Res.*, *87*, 457–468, 1982.

Holman, R. A., and T. C. Lippmann, Remote sensing of nearshore bar systems—Making morphology visible, Proceedings of the 20th International Conference on Coastal Engineering, pp. 929–944, Am. Soc. Civ. Eng., New York, 1987.

Holman, R. A., and A. H. Sallenger, Jr., High-energy nearshore processes, *Eos Trans. AGU*, *67*, 1369–1371, 1986.

Huntley, D. A., Guza, R. T., and E. B. Thornton, Field observations of surf beat, 1, Progressive edge waves, *J. Geophys. Res.*, *86*, 6451–6466, 1981.

Hwang, L.-S., and D. Divoky, Breaking wave set-up and decay on gentle slopes, Proceedings of the 12th International Conference on Coastal Engineering, pp. 377–389, Am. Soc. Civ. Eng., New York, 1970.

Keulegan, G. H., An experimental study of submarine sand bars, *Tech. Memo. 3*, 40 pp., U.S. Army Corps of Eng., Beach Erosion Board,1948.

Kuo, C. T., and S. T. Kuo, Effect of wave breaking on statistical distribution of wave heights, *Proc. Civ. Eng. Oceans, 3*, 1211–1231, 1974.

Lau, J., and B. Travis, Slowly varying Stokes waves and submarine longshore bars, *J. Geophys. Res., 78*, 4489–4497, 1973.

Lundall, A. C., Underwater depth determination by aerial photography, *Photogramm. Eng., 14*, 454–462, 1948.

Mason, C., W. A. Birkemeier, and P. A. Howd, Overview of DUCK85 nearshore processes experiment, Proceedings of the 20th International Conference on Coastal Engineering, pp. 818–833, Am. Soc. Civ. Eng., New York, 1987.

McCowan, J., On the solitary wave, *Philos. Mag. J. Sci., 32*, 45–58, 1891.

Miller, R. L., Role of vortices in surf zone prediction: Sedimentation and wave forces, beach and nearshore sedimentation, *Spec. Publ. Soc. Econ. Paleontol. Mineral., 24*, 92–114, 1976.

Okamoto, A., Wave influence in two media photogrammetry, *Photogramm. Eng., 48*, 1487–1499, 1982.

Oltman-Shay, J., and R. T. Guza, Infragravity edge wave observations on two California beaches, *J. Phys. Oceanogr., 17*, 644–663, 1987.

Sallenger, A. H., R. A. Holman, and W. A. Birkemeier, Storm-induced response of a nearshore bar system, *Mar. Geol., 64*, 237–257, 1984.

Shepard, F. P., Longshore bars and troughs, *Tech. Memo. 15*, 31 pp., U.S. Army Corps of Eng., Beach Erosion Board, 1950.

Short, A. D., Three dimensional beach-stage model, *J. Geol., 87*, 553–571, 1975.

Stoker, J. J., *Water Waves*, 567 pp., Interscience, New York, 1957.

Thornton, E. B., and R. T. Guza, Energy saturation and phase speeds measured on a natural beach, *J. Geophys. Res., 87*, 9499–9508, 1982.

Thornton, E. B., and R. T. Guza, Transformation of wave height distribution, *J. Geophys. Res., 88*, 5925–5938, 1983.

Thornton, E. B., and R. T. Guza, Surf zone currents and random waves: Field data and models, *J. Phys. Oceanogr., 16*, 1165–1178, 1986.

Wiegel, R. L., Recognition of underwater obstructions from aerial photography, *Wave Proj. Rep. HE-116-248*, 32 pp., Univ. of Calif., Berkeley, 1947.

R. A. Holman and T. C. Lippmann, College of Oceanography, Oregon State University, Corvallis, OR 97331.

(Received January 4, 1988;
accepted May 2, 1988.)